The impact of evaporation fractionation on the inverse estimation of soil hydraulic and isotope transport parameters

Tiantian Zhou, Jirka Šimůnek, Isabelle Braud, Paolo Nasta, Giuseppe Brunetti, Yi Liu

Publisher: Elsevier

Journal: Journal of Hydrology

DOI: 10.1016/j.jhydrol.2022.128100

The impact of evaporation fractionation on the inverse estimation of soil hydraulic and isotope transport parameters

Tiantian Zhou[1*], Jirka Šimůnek[1*], Isabelle Braud[2], Paolo Nasta[3], Giuseppe Brunetti[4], and Yi Liu[5]

[1] Department of Environmental Sciences, University of California Riverside, CA 92521, United States
[2] INRAE, Riverly, 5 Rue de la Doua, 69625 Villeurbanne, Cedex, France
[3] Department of Agricultural Sciences, AFBE Division, University of Naples Federico II, Portici (Naples), Italy
[4] Institute of Hydraulics and Rural Water Management, University of Natural Resources and Life Sciences, 1190, Vienna, Austria
[5] China Institute of Geo-Environment Monitoring, China Geological Survey, Beijing, 100081, China

Corresponding author: email: tzhou035@ucr.edu; jiri.simunek@ucr.edu

Abstract

Choosing a suitable process-oriented eco-hydrological model is essential for obtaining reliable simulations of hydrological processes. Determining soil hydraulic and solute transport parameters is another fundamental prerequisite. Research discussing the impact of considering evaporation fractionation on parameter estimation and practical applications of isotope transport models is limited. In this study, we analyzed parameter estimation results for two datasets for humid and arid conditions using the isotope transport model in HYDRUS-1D, in which we either did or did not consider fractionation. The global sensitivity analysis using the Morris and Sobol' methods and the parameter estimation using the Particle Swarm Optimization algorithm highlight the significant impact of considering evaporation fractionation on inverse modeling. The Kling-Gupta efficiency (KGE) index for isotope data can increase by 0.09 and 1.49 for the humid and arid datasets, respectively, when selecting suitable fractionation scenarios. Differences in estimated parameters propagate into the results of two practical applications of stable isotope tracing: *i*) the assessment of root water uptake (RWU) and drainage travel times (i.e., the time elapsed between water entering the soil profile as precipitation and leaving it as transpiration or drainage) in the lysimeter (humid conditions) and *ii*) evaporation estimation in a controlled experimental soil column (arid conditions). The peak displacement method with optimized longitudinal dispersivity provides much lower travel times than those obtained using the particle tracking algorithm in HYDRUS-1D. Considering evaporation fractionation using the Craig-Gordon (CG) and Gonfiantini models is likely to result in estimates of older water ages for RWU than the no fractionation scenario. The isotope mass balance method that uses the isotopic composition profile simulated by HYDRUS-1D while considering fractionation using the CG and Gonfiantini models, or the measured evaporation isotope flux, provides comparable results in evaporation estimation as the HYDRUS-1D water mass balance method and direct laboratory measurements. In contrast,

the no fractionation scenario reasonably estimates evaporation only when using the HYDRUS-1D water mass balance method. The direct use of simulated isotopic compositions in the no fractionation scenario may result in large biases in practical applications in the arid zone where evaporation fractionation is more extensive than in humid areas.

Keywords: HYDRUS-1D, Global sensitivity analysis; Particle swarm optimization; Water travel time, Temporal origin, Evaporation estimation

1 Introduction

Reliable water balance simulations in the vadose zone are important to understand and forecast the impact of anthropogenic disturbances such as global warming and land-use change on soil water storage, groundwater recharge, and evapotranspiration. A detailed mechanistic understanding of water fluxes in the vadose zone could support optimal and efficient management strategies for promoting the long-term sustainability of water resources and associated ecosystem functions (Penna et al., 2018). For example, the exact quantification of evaporation affects water availability for plants (Nelson et al., 2020) and constrains groundwater recharge (Condon et al., 2020). However, the conventional methods (e.g., pan experiments) for estimating evaporation fluxes often require extensive field monitoring of water flow, which is often time-consuming, expensive, labor-demanding, and affected by considerable uncertainty (Skrzypek et al., 2015).

Stable isotopes of hydrogen (^{2}H) and oxygen (^{18}O) are widely used to trace water fluxes across the critical zone and can be expressed as isotopic ratios, $^{2}H/^{1}H$ and $^{18}O/^{16}O$ by using the δ notation (i.e., $\delta^{2}H$ and $\delta^{18}O$). The isotopic composition of shallow soil water provides insights into evaporation fractionation characteristics. This information can be easily used to calculate corresponding evaporation fluxes. For example, Skrzypek et al. (2015) combined the equations for evaporation estimation based on the revised Craig-Gordon model (Craig and Gordon, 1965) and developed a software Hydrocalculator. Using this software, they estimated evaporation losses and validated its results using pan measurements. This method has been extended to soil evaporation estimation. For example, Sprenger et al. (2017) estimated that evaporation was about 5 and 10% of infiltrating water in the heath and Scots pine soils, respectively.

While the spatial origin of the water plants use has been widely studied (e.g., Allen et al., 2019), very little is known about its temporal origin (Brinkmann et al., 2018; Miguez-Macho and Fan, 2021). To

track water across the critical zone, we need to assess how fast water moves down to the soil profile bottom and when and how much water returns to the atmosphere through root water uptake (RWU). The premise is to accurately estimate travel times (TT) of irrigation/precipitation water (i.e., the time between water entering the soil profile as irrigation/precipitation and leaving it back to the atmosphere as transpiration or at the soil profile bottom as drainage).

The peak displacement method represents the most widespread technique to estimate travel time from the time difference between signals in soil water stable isotope time-series directly measured at specific soil depths (Chesnaux and Stumpp, 2018; Koeniger et al., 2016; Stumpp et al., 2012). However, this method is unfeasible when there is no pronounced peak correspondence between isotopic compositions of precipitation and drainage water samples. Another widely-used isotope-transport-based method is to inversely estimate the parameters for time-invariant TT distributions (TTDs) (e.g., Timbe et al., 2014) or time-variant StorAge Selection (SAS) functions (Benettin and Bertuzzo, 2018; Harman, 2015; Rinaldo et al., 2015) implemented in lumped hydrological models. Such oversimplified models are based on few soil and vegetation parameters but have limitations in describing transient conditions or simulating isotope transport (Sprenger et al., 2016a).

In contrast, isotope transport can be reliably simulated using the Richards equation-based hydrological models with appropriate soil and vegetation parameters and known boundary and initial conditions. However, direct measurements of soil hydraulic and transport parameters required by such models are time-consuming and labor-demanding. Therefore, such parameters are commonly obtained using inverse modeling by minimizing the errors between easily-measured state variables and fluxes (e.g., soil water contents and pressure heads at different soil depths or leachate water volumes) and corresponding model simulations (Hopmans et al. 2002; Mertens et al., 2006; Vrugt et al., 2008; Wollschläger et al., 2009; Wöhling and Vrugt, 2011).

Nevertheless, it is not always necessary to account for all model parameters in parameter optimization since some can be fixed as they can be either determined experimentally or have a minor impact

on the model output. The latter can be determined using the global sensitivity analysis (GSA). The Sobol' and Morris methods are among the two most widespread GSA methods (Liu et al., 2020). The Sobol' method provides the most accurate sensitivity indices, but it requires several model runs and is thus computationally intensive (Gatel et al., 2019). In contrast, the Morris method cannot yield the order of the most sensitive parameters as accurately as the Sobol' method, but its computational cost is much lower, and it can still pinpoint the most influential parameters (Campolongo et al., 2007; Herman et al., 2013).

Many inverse modeling algorithms can be used for parameter estimation. For example, the Levenberg-Marquardt Optimization (LMO) proved to be very efficient and was, therefore, implemented in HYDRUS (Šimůnek et al., 2008). However, the LMO is sensitive to the initial parameter values provided by the user and often falls into local instead of global minimum (Brunetti et al., 2016). Thus, global optimization algorithms, such as Particle Swarm Optimization (PSO), have become more widespread over the last decades (e.g., Vrugt and Robinson, 2007).

When optimizing isotope transport parameters via inverse modeling, isotopic compositions from multiple soil depths must be included in the objective function and combined with other state variables and fluxes. For example, research shows that the model calibration can be improved by simultaneously considering stable isotopes and soil moisture information (Sprenger et al., 2015; Groh et al., 2018; Mattei et al., 2020). However, the correct model structure is a fundamental prerequisite to obtaining successful simulations. In particular, research discussing the impact of considering evaporation fractionation on parameter estimation and practical applications of isotope transport models is limited (Penna et al., 2018). Therefore, we pose two scientific questions. First, how will the consideration of evaporation fractionation affect the parameter estimation results of the isotope transport model? Second, how will this effect propagate into practical applications such as water travel times and evaporation estimation?

To answer these questions, we compare the parameter estimation results obtained using the isotope transport model in HYDRUS-1D (Zhou et al., 2021) that does or does not consider evaporation fractionation for two available datasets: 1) a 150-cm-thick layered soil profile in a lysimeter under humid climate where

evaporation fractionation is negligible; 2) a 35-cm-thick soil column subject to evaporation where evaporation fractionation process is dominant. The accuracy of the parameterization obtained by the PSO algorithm is assessed based on its ability to reproduce measured water fluxes and isotope transport data. The parameters estimated while considering (or not) evaporation fractionation are then used to calculate travel times and evaporation.

2 Materials and Methods

Two experimental datasets are considered in this study. The first dataset is collected using a field lysimeter (150-cm-thick layered soil profile) located in Austria under humid climate conditions (Stumpp et al., 2012) (Section 2.1.1). The second dataset is collected using a 35-cm-thick soil column (in France) subject to evaporation to mimic arid climate conditions (Braud et al., 2009a) (Section 2.1.2). Numerical simulations of water flow and isotope transport (with and without evaporation fractionation) are implemented in HYDRUS-1D. The modeling setup is briefly described in Section 2.2 and Method S1 in the Supplementary Material. The sensitivity analysis based on the Sobol' and Morris methods is performed to evaluate the interactions between soil hydraulic and solute transport parameters and the impact of multiple measured data types (Section 2.3, Method S2, and Results S1~S2). The accuracy of the parameterization obtained by the PSO algorithm is assessed based on its ability to reproduce the observed data (Sections 2.4, 3.1.1, and 3.2.1). The parameters estimated while considering or not considering evaporation fractionation are then used to calculate travel times and evaporation and quantify the impact of their different estimates (Sections 2.5, 2.6, 3.1.2, and 3.2.2). The effects of varying climate conditions and estimation methods are then compared and illuminated (Section 4).

The schematic outline of the different methods used is shown in Fig. 1. The description of relevant symbols and acronyms is given in the Appendix.

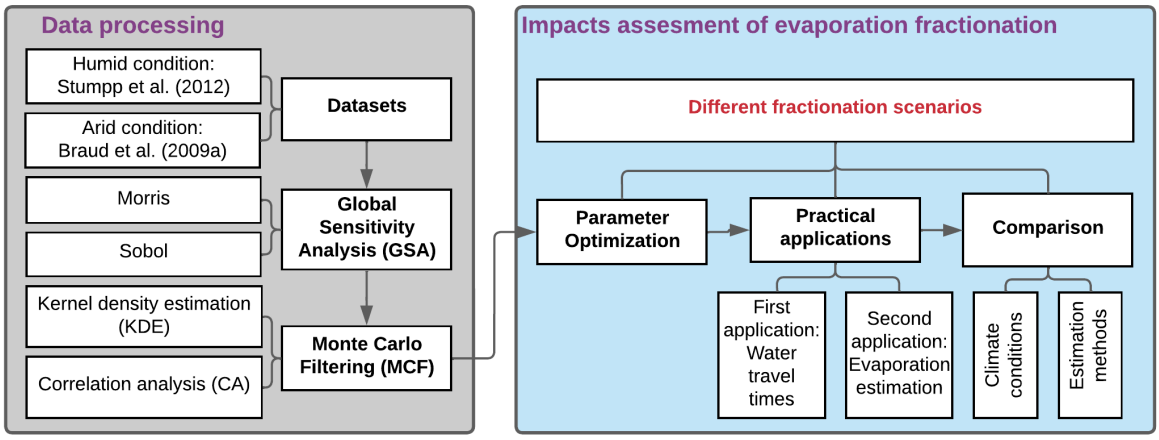

Figure 1. Schematic outline of methods used.

2.1 Site description and data availability

2.1.1 Stumpp et al. (2012) dataset

The first dataset is taken from the lysimeter 3 of Stumpp et al. (2012) (available at https://www.pc-progress.com/en/Default.aspx?h1d-lib-isotope). The field experiment was conducted in a humid region located at the research area of the HBLFA (Höhere Bundeslehr- und Forschungsanstalt für Landwirtschaft) Raumberg-Gumpenstein, in Gumpenstein, Austria. This area has a mean annual temperature of 6.9 °C and average annual precipitation (P) of 1035 mm. The annual potential evapotranspiration (ET_0) (for grass reference) during the experiment period (May 2002 to February 2007) calculated by the Penman-Monteith equation is about 557 mm, and the corresponding aridity index (P/ET_0) is about 1.86, corresponding to a humid climate class (Liang, 1982). The cylindrical lysimeter (with a depth of 150 cm and a surface area of 10000 cm^2) was embedded in a rainfed agricultural field (Cambisol) planted with winter rye and fertilized with liquid cattle slurry.

The observation period was from May 2002 to February 2007 (1736 days). Table S1 shows the summary of the observed data. The temporal distribution of P, ET_0, soil surface temperature (T_s), air relative humidity (RH), and leaf area index (LAI) during the simulation period are shown in Fig. 2. More details

about data acquisition, including meteorological parameters and root water uptake information, can be found in Stumpp et al. (2012).

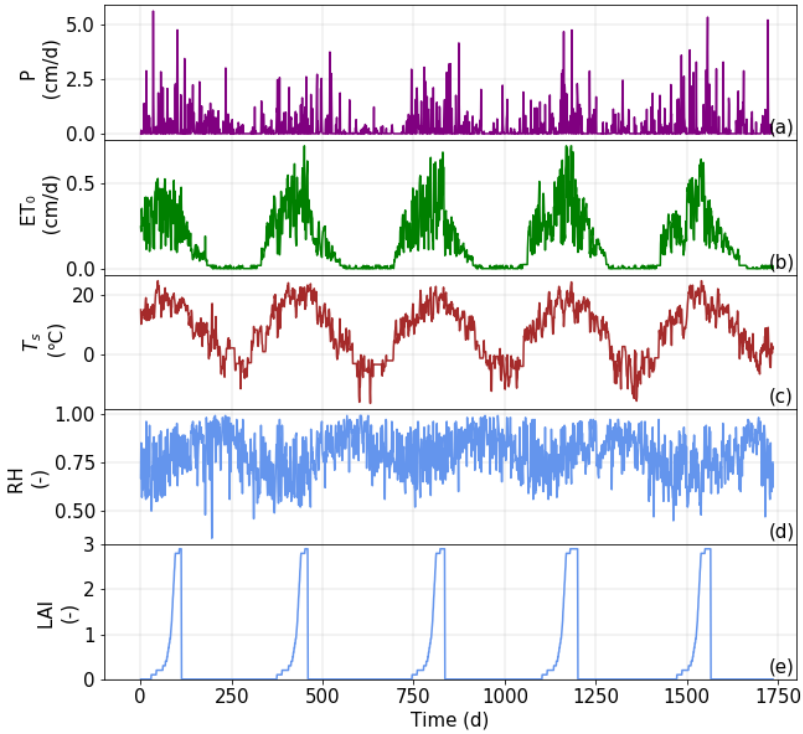

Figure 2. The temporal distribution of precipitation (P) (a), potential evapotranspiration (ET_0) (b), soil surface temperature (T_s) (c), air relative humidity (RH) (d), and leaf area index (LAI) (e) during the simulation period for the Stumpp et al. (2012) dataset (adapted from Stumpp et al., 2012).

2.1.2 Braud et al. (2009a) dataset

Braud et al. (2009a) designed a RUBIC IV experiment that started on April 11, 2005, corresponding to Day of the Year (DoY) 101, and lasted 338 days. The experiment consisted of 6 columns, 12 cm in diameter and 35 cm in height. The soil columns were filled with a silt loam collected at the field station of Lusignan, France, and wetted using demineralized water of the known isotopic composition. The bottom was closed by clay marbles. The soil was initially saturated and subject to evaporation only. Dry air was simultaneously injected over all six columns. The isotopic composition of the air changed due to water vapor released by evaporation from soil columns. The air was finally trapped in a cryoscopic device, which

allowed the determination of evaporation fluxes from bare soil columns and the corresponding isotopic composition of the water vapor under non-steady-state conditions. More details about the experimental setup can be found in Figs. 1~2 of Braud et al. (2009a). The data collected in Column 2, ending at DoY 264, were analyzed in this study.

Thirteen variables were measured continuously at a frequency of about 15 minutes to assess the water balance of the soil column. These variables included the room temperature, the atmospheric pressure, the absolute pressure of the dry air before it entered the soil column, air mass flow for the humidity control above the soil column, the mass of the soil column, air temperature and humidity at the outlet of the soil column, the temperatures of the cryoscopic trapping downstream and upstream of the columns, and the air temperature and residual air humidity at the outlets of two cold traps. The vapor was trapped twice a day during the first three months and only once a day after that once evaporation decreased. Soil column 2 was dismantled on September 21, 2005 (DoY 264) to sample liquid water and measure the gravimetric soil water content. More details about data acquisition can be found in Braud et al. (2009a). The temporal distributions of the evaporation flux (E), the isotopic composition of the evaporation flux (δ_E), outlet air temperature (T_{air}), and outlet air relative humidity (RH) during the simulation period are shown in Fig. 3.

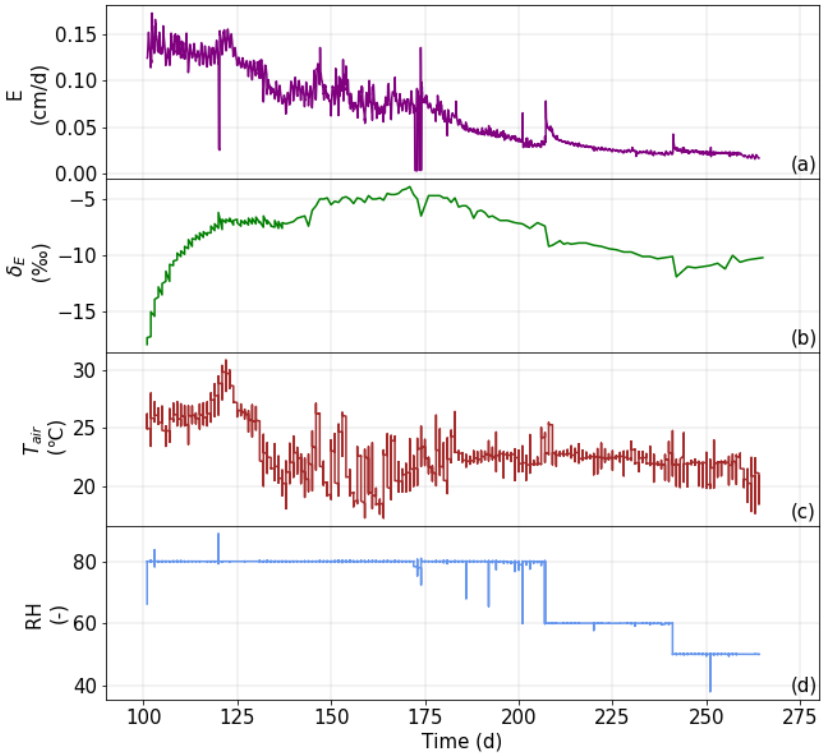

Figure 3. Time series of the evaporation flux (E) (a) isotopic composition of the evaporation flux (δ_E) (b), outlet air temperature (T_{air}) (c), outlet air relative humidity (RH) (d), during the simulation period for the Braud et al. (2009a) dataset (adapted from Braud et al., 2009a).

2.2 Model setup

The HYDRUS-1D model modified by Zhou et al. (2021) to simulate the transport of soil water isotopes while considering evaporation fractionation was used in this study. A brief summary of the model setup, including the governing equations (without and with vapor flow for the Stumpp et al. (2012) and Braud et al. (2009a) datasets, respectively), boundary conditions (BCs), and model inputs is shown in Figs. 4~5. More details can be found in Zhou et al. (2021).

2.2.1 Stumpp et al. (2012) dataset

The soil profile was 150 cm deep and was discretized into 151 nodes. It consisted of three different soil horizons (0 ~ 29 cm; 30 ~ 89 cm; 90 ~ 150 cm). The initial pressure head profile was assumed to be at hydrostatic equilibrium with the pressure head h=−150 cm at the soil surface. The weighted average $\delta^{18}O$ of precipitation (-9.5‰) and estimated temperature (20 ℃) were used as initial conditions.

The atmospheric (with a surface layer) and seepage face boundary conditions (BC) were used for water flow at the upper and lower boundaries, respectively. The temperature BC was used for heat transport at both boundaries. In this humid condition example, evaporation fractionation was limited to the soil surface due to the lack of the vapor phase within the soil. The solute flux and zero concentration gradient BCs were used for isotope transport at the upper and lower boundaries, respectively. The isotope flux associated with evaporation was calculated either assuming no fractionation or using the Craig-Gordon or Gonfiantini fractionation models (hereafter referred to as Non_Frac, CG_Frac, and Gon_Frac, respectively). The Non_Frac scenario calculated the isotope flux of evaporation by assuming that the isotopic composition of the evaporation flux was the same as that of surface soil water. The isotopic composition of the atmospheric water vapor (δ_A) in the CG_Frac scenario was estimated based on its equilibrium relationship with the isotopic composition of rainfall (Skrzypek et al., 2015). The Gon_Frac scenario was simplified (without the need for the isotopic composition of the atmospheric water vapor) to consider fractionation (Zhou et al., 2021). A detailed description of the CG and Gonfiantini models can be found in Method S1. For simplification, only equilibrium fractionation was considered at the soil surface since kinetic fractionation could be neglected in this example (Zhou et al., 2021). In other words, the kinetic fractionation coefficient (n_k) in Eq. (11) of Zhou et al. (2021) was set to 0, and thus the kinetic fractionation factor at the soil surface (α_i^k) in the CG_Frac and Gon_Frac scenarios (Eqs. S2, S3) was equal to 1.

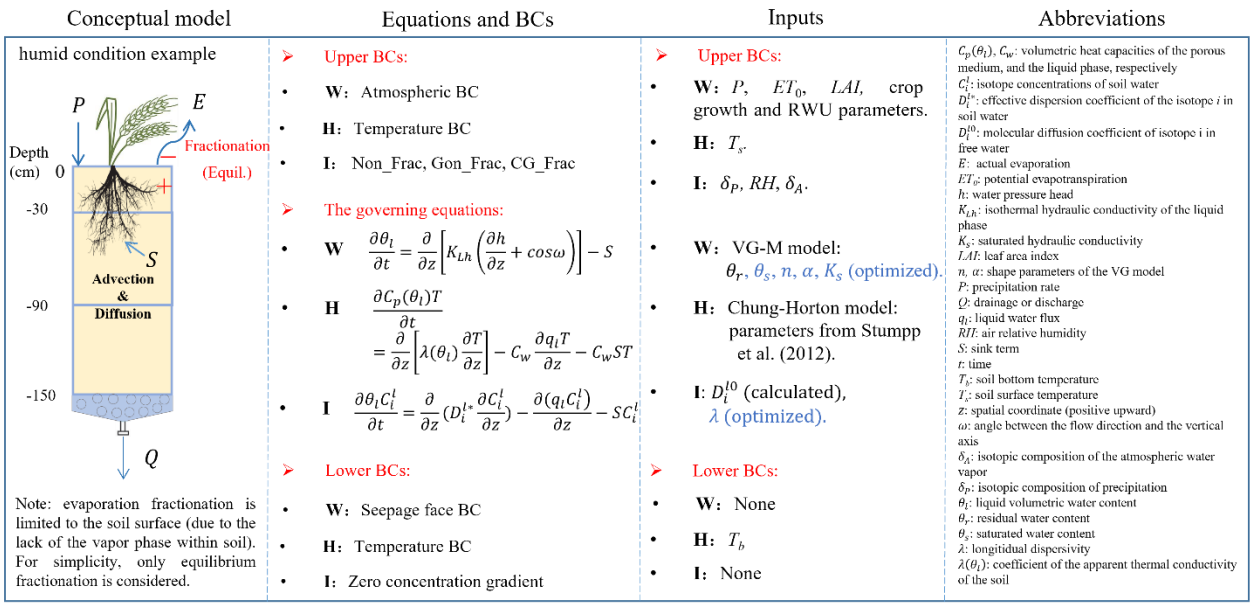

Figure 4. Model setup for the Stumpp et al. (2012) dataset. Note that "W," "H," and "I" represent water flow, heat transport, and isotope transport, respectively.

2.2.2 Braud et al. (2009a) dataset

The simulated soil profile was 35 cm deep and was discretized into 132 nodes following Braud et al. (2009a). The soil column was initially almost fully saturated, with the measured initial pressure head increased linearly from −1 cm at the soil surface to 35 cm at the soil profile bottom. The observed initial soil temperature and $\delta^{18}O$ were 24.25 ℃ and -6.34‰, respectively.

The temperature BC was used for heat transport at both surface and bottom boundaries, using temperatures measured at 2.5 and 24 cm depths, respectively. The atmospheric and zero flux BCs were used for water flow at the upper and lower boundaries, respectively. The measured evaporation flux, E was used as the upper BC for water flow. In this arid condition example, evaporation fractionation occurred both at the soil surface and within the soil due to the existence of the vapor phase. The stagnant air layer BC (which had been modified to account for evaporation fractionation) and zero flux BC were used for isotope transport

at the upper and lower boundaries, respectively. The surface isotope flux associated with evaporation was calculated either assuming no fractionation, using the Craig-Gordon or Gonfiantini fractionation models, or using the measured values (hereafter referred to as Non_Frac, CG_Frac, Gon_Frac, and Meas_Frac, respectively). The Non_Frac scenario calculated the isotope flux of evaporation by assuming that its isotopic composition was the same as that of surface soil water (i.e., no fractionation at the soil surface), and equilibrium and kinetic fractionation factors within the soil (α^+, α_i^D) were equal to 1 (i.e., no fractionation within the soil). The theory of CG_Frac and Gon_Frac scenarios was explained in Method S1. For simplification, the kinetic fractionation coefficient n_k in Eq. (11) of Zhou et al. (2021) was set to 1, and thus the kinetic fractionation factor at the soil surface (α_i^k) in the CG_Frac and Gon_Frac scenarios (Eqs. S2, S3) was equal to 1.0324. The measured isotopic composition of the outlet water vapor, δ_E, was used in the Meas_Frac scenario to calculate the surface isotope flux E_i corresponding to the evaporation flux E. More details about how upper boundary fluxes were calculated can be found in Braud et al. (2009a).

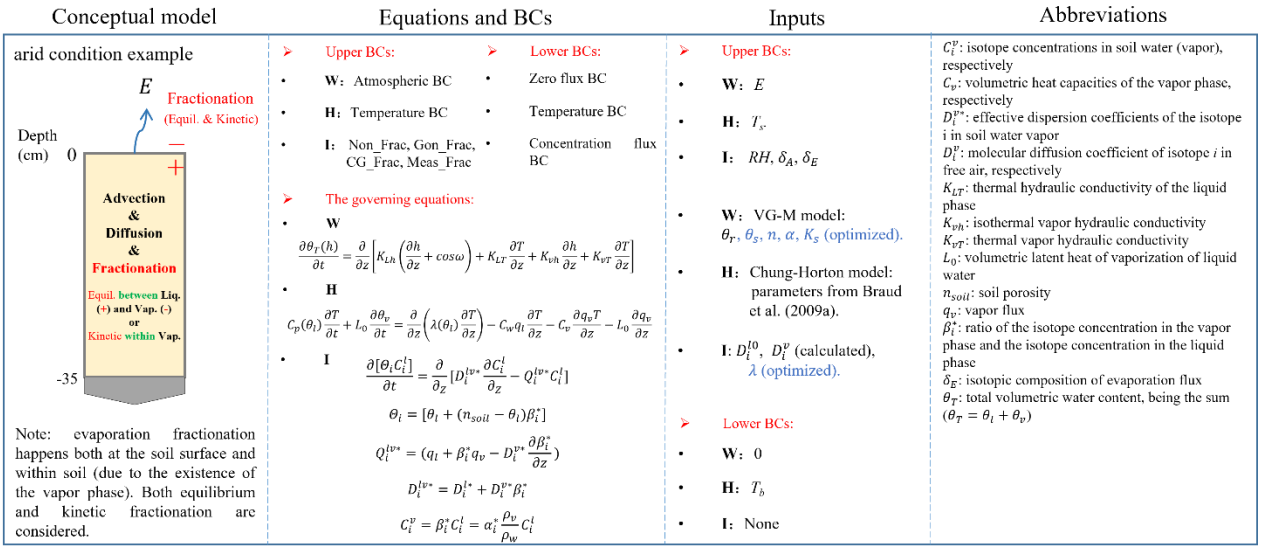

Figure 5. Model setup for the Braud et al. (2009a) dataset. Note that "W," "H," and "I" represent water flow, heat transport, and isotope transport, respectively.

2.3 Global sensitivity analysis

Five soil hydraulic parameters (i.e., θ_r, θ_s, n, α, and K_s) need to be optimized for each layer of the soil profile to simulate water flow using the HYDRUS-1D model. The residual water content θ_r was set to zero to reduce the number of fitting parameters. To simulate isotope transport in the soil, the longitudinal dispersivity λ also needs to be optimized. Since only the isotopic composition of the lysimeter discharge was measured in the Stumpp et al. (2012) dataset, the dispersivity of three individual soil layers cannot be estimated. Therefore, only one longitudinal dispersivity for the entire lysimeter was estimated. Therefore, the total number of parameters *p* was 13 and 5 for the Stumpp et al. (2012) and Braud et al. (2009a) datasets, respectively. The global sensitivity analysis (GSA) using both Morris and Sobol' methods was conducted in this study to determine the most influential parameters and their interactions. The detailed description of these two methods is shown in Method S2 in the Supplementary Material.

The sensitivity analysis was conducted using Python's Sensitivity Analysis Library (SALib) (Herman and Usher, 2017). The script produces the input parameter space, overwrites the input parameters file, and runs the executable module of HYDRUS-1D. For each simulation of the Stumpp et al. (2012) dataset, five Kling-Gupta efficiency (KGE) indices for different evaluation indicators were calculated, including for the time series of the bottom water flux (KGE_bf), the soil water content at different depths (KGE_wc), the bottom water isotopic composition (KGE_wi), the water retention curves (KGE_rc), and the average of the four KGE values (KGE_avg). For each simulation of the Braud et al. (2009a) dataset, three Kling-Gupta efficiency (KGE) indices for different evaluation indicators were calculated, including the final soil water content profile (KGE_wc), the final water isotopic composition profile (KGE_wi), and the average of the two KGE values (KGE_avg). The KGE index compares the correlation coefficient (r), the ratio of mean values (β), and the ratio of variances (γ) between simulated and observed data. The value of the KGE index is always smaller or equal to 1. The higher the KGE value, the better fit between the simulated and observed values. The positive and negative KGE values are often considered "good" and "bad" solutions (Knoben et al., 2019).

$$\mathrm{KGE} = 1 - [(1 - r)^2 + (1 - \beta)^2 + (1 - \gamma)^2]^{0.5} \quad (1)$$

If a HYDRUS-1D run was not finished within a prescribed time (i.e., 30 s and 60 s for the Stumpp et al. (2012) and Braud et al. (2009a) datasets, respectively) or the length of the modeled hydrograph was shorter than the total simulation period (1736 and 163 days for the Stumpp et al. (2012) and Braud et al. (2009a) datasets, respectively), it was considered non-convergent. The run was then terminated, and a large negative value (−1E+7) was prescribed to the objective function.

Non-convergent runs in GSA are a frequent problem when using nonlinear environmental/hydrological models, and there are no clear indications on how to handle these "unfeasible" points (Razavi et al., 2021). Removing or skipping them alters the sampling trajectory and can result in biased conclusions, especially if non-convergent runs lie in informative regions of the parameter space. Recently, Sheikholeslami et al. (2019) compared strategies such as median substitution, single nearest-neighbor, or response surface modeling (Brunetti et al., 2017) to fill in for model crashes. Their results show that interpolating non-convergent runs with a radial basis function trained in the vicinity of that point leads to reliable results and outperforms other strategies. We implemented a similar approach in the present work but with important differences. In particular:

1. For each non-convergent point, we calculated its Euclidean distance from all other convergent points in the GSA sample.
2. Convergent points were ordered in ascending order (i.e., from the closest to the farthest).
3. The 100 closest convergent points were used to train a response surface surrogate based on the Kriging Partial Least Squares method (KPLS) (Bouhlel et al., 2016), which outperforms traditional kriging on high-dimensional problems.
4. The trained KPLS surrogate was finally used to interpolate non-convergent runs in the original GSA sample.

The use of multiple localized surrogates allowed for better reconstruction of the topological features of the response surface in the vicinity of the non-convergent points.

In this study, the global sensitivity analysis was combined with the Monte Carlo filtering to identify reduced ranges of parameters with good solutions for subsequent parameter optimization. Potential solutions were filtered into good solutions with KGE > 0.0 and bad solutions with KGE ≤ 0.0. Kernel density estimation (KDE) plots were then used to identify areas with high-density good solutions, while the correlation analysis was conducted to determine interactions between parameters and may help reduce the input factor space. More details can be found in Brunetti et al. (2016). This type of procedure shares multiple similarities with the Generalized Likelihood Uncertainty Estimation (GLUE) proposed by Beven et al. (2001). The joint use of the GSA sample with the GLUE approach [i.e., GSA-GLUE (Ratto et al., 2001)] allows for obtaining a rough assessment of the parameters uncertainty and successful estimates of soil hydraulic parameters (e.g., Brunetti et al., 2018).

2.4 Parameter optimization

The Particle Swarm Optimization (PSO) algorithm was used in this study for parameter optimization. In the PSO, a swarm of candidate solutions is moved around in the search space according to a few equations. The movement of the particles is guided by the optimal position of themselves and the whole swarm. Once improved positions are discovered, they are used to guide the swarm's movement. This process is repeated until the global optimal position that all particles tend to follow is found (Shi and Eberhart, 1998).

The PSO parameters (cognitive parameter c_1=-0.267; social parameter c_2=3.395; inertia-weight w=-0.444) from Brunetti et al. (2016) were used in this study. The number of particle swarm and iterations are 40 and 200, respectively.

The PySwarm Library in Python was used for the PSO. The process was similar to the GSA, except that reduced ranges of parameters were used. In this way, the number of potential local minima is reduced, and the convergence improves. Only the set of parameters leading to the maximum KGE_avg (i.e., minimum 1-KGE_avg as the objective function) was retained as optimized parameters.

330

331 **2.5 First practical application: Calculation of drainage and RWU travel times**

332 **2.5.1 The peak displacement (isotope-transport-based) method**

333 The peak displacement method estimates travel times from the time lag between signals in the
334 measured input (rainfall isotopic composition) and output (drainage isotopic composition) isotope time
335 series. In the Stumpp et al. (2012) dataset, a pronounced correspondence was observed between the depleted
336 precipitation peak in the winter (November 18, 2005, to April 14, 2006) and the lysimeter discharge. The
337 mean drainage travel time t_o^* [T], accounting for dispersion effects, can be calculated by the mean peak
338 isotopic composition lag time t_m^* [T] using Eq. 2:

$$t_o^* = \frac{t_m^*}{\sqrt{1 + (3\frac{\lambda}{L})^2} - 3\frac{\lambda}{L}} \quad (2)$$

339 where L is the lysimeter length [L]. More details can be found in Stumpp et al. (2012). In this study, t_m^*
340 from Stumpp et al. (2012) and dispersivities λ optimized using HYDRUS-1D assuming different
341 fractionation scenarios were used.

342 **2.5.2 The particle tracking (water-flow-based) method**

343 The particle tracking algorithm is based on the water mass balance calculation. The initial position
344 of the particles is defined using the initial water content distribution. Depending on the
345 precipitation/irrigation inputs, the particles may be released at the soil surface and leave at the soil profile
346 bottom. In this study, the input parameters w_{Stand} (the initial distribution) and w_{Prec} (the upper BC distribution)
347 for the particle tracking algorithm were set to 10 cm and a negative number (which triggers the option of
348 releasing particles with each rain event), respectively. More details about the particle tracking algorithm can
349 be found in Šimůnek (1991) or Zhou et al. (2021).

350 When knowing the positions of the particles at different times, the residence time (*RT*) and locations
351 of water from all precipitation/irrigation events can be obtained, i.e., the residence time distribution (*RTD*).

Note that the particle travel time (*TT*) is the sum of the particle age (i.e., residence time) and life expectancy (i.e., time to reach the destination). The former is the time elapsed since the particle release, while the latter is the remaining time before the particle reaches the outlet (Benettin et al., 2015). Therefore, when the particles leave the lysimeter bottom or as root water uptake (RWU), their residence times can be called drainage or RWU travel times, respectively. The particle tracking module additionally assesses RWU between two neighboring particles as a function of time. When particles are released for each precipitation event, we can precisely evaluate the contribution of each precipitation event to RWU at different times. We can then infer the temporal origin of RWU by synthesizing this information. Different fractionation scenarios with the soil hydraulic parameters optimized using HYDRUS-1D were used to run the particle tracking module to calculate drainage and RWU travel times.

2.6 Second practical application: Calculation of evaporation flux

2.6.1 The water-flow-based method

Braud et al. (2009a) calculated evaporation using three methods. The first method determines the evaporation rate by continuously measuring the vapor flux and humidity at the outlet of the soil column. The second method obtains the evaporation rate by repeatedly weighing the soil column. Finally, the third method determines the evaporation rate by weighting the mass of the frozen water trapped at the outlet of the soil column. These three methods are hereafter referred to as direct measurement, column weighting, and trapped volume, respectively. This study presents these results also as the reference for other methods. More details can be found in Braud et al. (2009a). Another water-flow-based method used in this study to calculate water flux components was to analyze the water mass balance simulated in HYDRUS-1D (e.g., Sutanto et al., 2012).

2.6.2 The isotope-transport-based method

For an isolated water volume with an initial isotopic composition, δ_0 (‰) evaporating into the atmosphere, the isotopic composition of the residual liquid water δ_s (‰) can be calculated as (Benettin et al., 2018):

$$\delta_s = (\delta_0 - \delta^*)(1 - F_E)^{xm} + \delta^* \quad (3)$$

where δ^* (‰) is the limiting isotopic composition that would be approached when water is drying up, xm is the temporal enrichment slope (–), and F_E is described below.

Eq. (3) is based on the isotope mass balance equations of Gonfiantini (1986) and the isotopic composition of the evaporation flux estimated by the Craig–Gordon model (Craig and Gordon, 1965). More details about the derivations can be found in Gonfiantini (1986). This equation implies that the isotopic composition of soil water only changes due to evaporation fractionation. The ratio of the evaporation loss to the initial water storage (F_E) can be then estimated as (Sprenger et al., 2017):

$$F_E = 1 - [\frac{(\delta_s - \delta^*)}{(\delta_0 - \delta^*)}]^{\frac{1}{xm}} \quad (4)$$

The two variables δ^* and xm can be calculated as (Benettin et al., 2018):

$$\delta^* = \frac{(RH \cdot \delta_A + \varepsilon_k + \varepsilon^+/\alpha^+)}{(RH - 10^{-3}(\varepsilon_k + \varepsilon^+/\alpha^+))} \quad (5)$$

$$xm = \frac{(RH - 10^{-3}(\varepsilon_k + \varepsilon^+/\alpha^+))}{(1 - RH + 10^{-3}\varepsilon_k)} \quad (6)$$

where δ_A (‰) is the isotopic composition of the atmospheric water vapor, RH is the air relative humidity, α^+ (–) is the dimensionless equilibrium fractionation factor, while ε^+ (‰) and ε_k (‰) are equilibrium and kinetic fractionation enrichments, respectively. Details about the calculation procedure for these parameters (α^+, ε^+, ε_k) can be found in Benettin et al. (2018) or Zhou et al. (2021). The equivalent kinetic fractionation factor within the soil (α_i^D) used to calculate ε_k was optimized manually to get the best match of F_E with those from water-flow-based methods in Section 2.6.1.

The fraction of water that evaporated before the end of the Braud et al. (2009a) experiment was calculated in this study. Average measured values of RH, T_{air}, T_s, and δ_0 during the experiment, and the final isotope profile simulated using HYDRUS-1D were used in the above equations.

3 Results

3.1 Stumpp et al. (2012) dataset analysis

3.1.1 Parameter optimization and model performance

The global sensitivity analysis and Monte-Carlo filtering results for the Stumpp et al. (2012) dataset are shown in the Results S1 section of the Supplementary material. Overall, soil hydraulic parameters of different layers had comparable impacts on the model outputs. The order of sensitive parameters is: shape parameters of the water retention function, namely n, and α, saturated water content θ_s, saturated hydraulic conductivity K_s, and dispersivitie λ. The final optimized soil hydraulic and solute transport parameters and corresponding KGEs are shown in Table 1. Considering evaporation fractionation impacted parameter estimation significantly, especially in the optimization of the soil saturated hydraulic conductivity, K_s, and shape parameter, α. Overall, the water retention and soil hydraulic conductivity curves (Fig. S8) differed greatly between different fractionation scenarios in the third layer, but were relatively similar in the first and second layers. The water retention curve in the Gon_Frac scenario best matched the measured one, but did not outperform those from the CG_Frac and Non_Frac scenarios, as seen from the KGE_rc values in Table 1. Compared with the CG_Frac and Gon_Frac scenarios, the water retention curve in the Non_Frac scenario had a steeper decline and a lower saturated water content in the third layer, while it became more gradual with higher saturated water contents in the first and second layers. However, the Non_Frac scenario always produced higher hydraulic conductivities than the CG_Frac and Gon_Frac scenarios (Note that the Non_Frac scenario also had higher hydraulic conductivities in the third layer because of relatively higher matric potentials).

The fits for different fractionation scenarios are shown in Fig. 6. The isotopic composition of the lysimeter discharge remained the same for different fractionation scenarios during about the first 150 days

and started deviating after this time, but the trends were still similar except for some vertical shifts. Different fractionation scenarios resulted in a similar average fitting performance (KGE_avg) (within 0.03). The Non_Frac scenario had the highest KGE_wi (i.e., for water isotopic composition), followed by the CG_Frac scenario, while the Gon_Frac scenario performed the worst. The difference between KGE_wi indices for different fractionation scenarios was within 0.09.

Table 1. Optimized parameters and Kling-Gupta efficiency (KGE) indices (bf, wc, wi, and avg refer to the bottom flux, water content, water isotopic composition, and average, respectively) for different fractionation scenarios (Non_Frac, CG_Frac, and Gon_Frac) (for the Stumpp et al. (2012) dataset).

Fractionation scenario	z	θ_r	θ_s	α	n	K_s	λ	KGE_bf	KGE_wc	KGE_wi	KGE_rc	KGE_avg
	cm	cm^3/cm^3	cm^3/cm^3	cm^{-1}	-	cm/d	cm					
Non_Frac	0–30	0	0.31	0.010	1.19	83.6	5.00	0.99	0.47	0.59	0.87	0.73
	31–90	0	0.43	0.293	1.11	1131.71						
	91–150	0	0.30	0.009	1.91	85.16						
CG_Frac	0–30	0	0.30	0.020	1.15	220.00	5.00	0.99	0.54	0.58	0.89	0.75
	31–90	0	0.41	0.300	1.11	287.24						
	91–150	0	0.30	0.082	1.10	220.00						
Gon_Frac	0–30	0	0.30	0.026	1.14	220.00	6.02	0.99	0.45	0.50	0.92	0.72
	31–90	0	0.40	0.298	1.11	191.89						
	91–150	0	0.35	0.300	1.12	220.00						

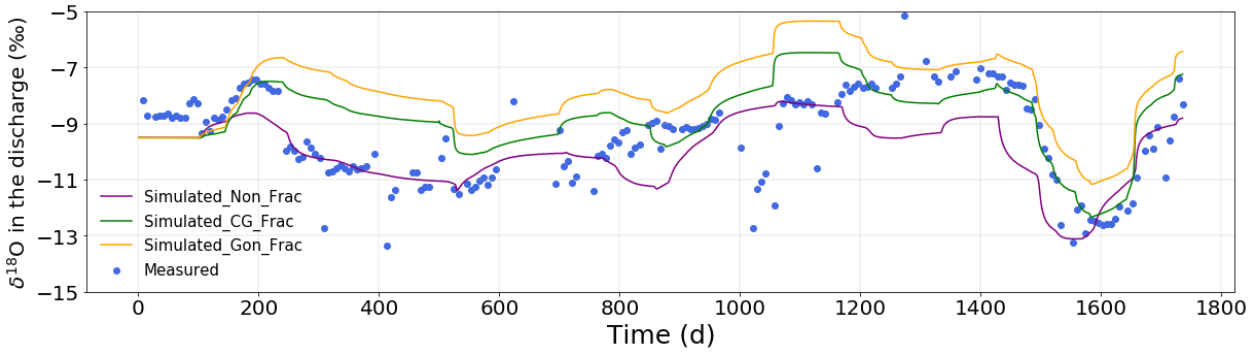

Figure 6. Measured (symbols) and simulated discharge ^{18}O isotopic compositions for different fractionation scenarios (for the Stumpp et al. (2012) dataset).

3.1.2 First practical application: Drainage travel times and RWU temporal origin

The mean travel times (*MTT*s) of drainage (i.e., from the surface to the bottom) estimated by the peak displacement method are shown in Table 2. The *MTT*s were 251.9, 251.9, and 257.1 days for the Non_Frac, CG_Frac, and Gon_Frac scenarios, respectively. The consideration of fractionation using the Gonfiantini model slightly overestimated the travel times compared to the Non_Frac scenario. However, the difference was not very evident (within 6 days) for different fractionation scenarios.

Table 2. Estimated mean travel times of drainage (t_0^*) and mean water fluxes (v_0^*) for different fractionation scenarios (Non_Frac, CG_Frac, and Gon_Frac) using different methods (peak displacement and particle tracking).

Method	Fractionation scenario	t_0^* (d)	v_0^* (mm/d)	Ratio of t_0^* compared to t_0^* for Non_Frac
Peak displacement	Non_Frac	251.9	5.95	
	CG_Frac	251.9	5.95	0%
	Gon_Frac	257.1	5.83	2.06%
Particle tracking	Non_Frac	297.5	5.04	
	CG_Frac	356.8	4.20	19.93%
	Gon_Frac	369.9	4.05	24.33%

Fig. S9 shows the spatial-temporal distribution of particles simulated using the soil hydraulic parameters estimated considering different fractionation scenarios. The residence time distribution (*RTD*) of soil water is displayed in Fig. 7. The mean residence time (*MRT* – the mean of *RT*s averaged over the entire simulation duration) increased with soil depth in all scenarios due to a time lag involved in water transfer. The *MRT*s for the Non_Frac scenario for depths of 30, 70, and 110 cm were 82.1, 138.2, and 203.6 days, respectively. The *MRT*s for the CG_Frac scenario for 30, 70, and 110 cm depths were 69.9, 170.0, and 258.5 days, respectively. Finally, the *MRT*s for the Gon_Frac scenario for 30, 70, and 110 cm depths were 80.6, 174.3, and 270.6 days, respectively. In terms of temporal distribution, *RT*s showed five distinct seasonal cycles. Specifically, they had a trough after every rainy season and a peak after every dry season,

showing a pronounced lag effect. In other words, *RT*s were determined by the trade-off between precipitation input and evapotranspiration removal.

Corresponding travel times of drainage are shown as probability density distribution histograms in Fig. S10 and summarized in Table 2. The means (and standard deviations) of travel times were 297.5 (79.96), 356.8 (104.29), and 369.9 (101.24) days for the Non_Frac, CG_Frac, and Gon_Frac scenarios, respectively. The particle tracking method produced significantly higher travel times (by about 89 days) than the peak displacement method. Similarly, considering fractionation using the CG_Frac and Gon_Frac scenarios led to longer travel times (*TT*s) than the Non_Frac scenario. In addition, the difference was very evident (reached 78 days) for different scenarios.

To further explore and quantify the *RTD* differences when considering different fractionation models, the temporal origin of RWU is plotted in Fig. 8. Fig. 8 shows the monthly transpiration sums in the upper panels and fractional contributions of water of a certain age/origin to these monthly transpiration sums in the lower panels. Note that the amount and temporal distribution of transpiration were similar under different fractionation scenarios (54.95, 53.91, and 54.03 cm for Non_Frac, CG_Frac, and Gon_Frac, respectively). Therefore, only the temporal distribution of transpiration in the Non_Frac scenario is displayed. As for the age distribution of RWU, for example, in the Non_Frac scenario, the yellow line in 2002 indicates that about 29% of the water taken up by roots in August was older than May, while the remaining 71% was from May~August of 2002 (5% from June, 16% from July, and 50% from August). More details about how to read the age distribution of RWU can be found in Fig. 5 of Brinkmann et al. (2018).

The maximum water age for RWU for different fractionation scenarios was almost the same, about 300 d in October 2003, 330 d in September 2004, 270 d in November 2005, and 180 d in February 2006, except for 240 d in December 2004 and 180 d in February of 2005 for the Non_Frac scenario. These results were consistent with water residence times at the maximum rooting depths in Fig. 7. However, different fractionation scenarios had relatively large impacts (up to three months) on the minimum water age for

RWU. The most obvious example was the 2003 growing season (a relatively dry year with less precipitation, as shown in Fig. 2). The minimum water age for RWU in 2003 was within about a month for the Gon_Frac scenario and 120 d (February) for the Non_Frac and CG_Frac scenarios. In addition, the dynamics of fractional monthly contributions to RWU also varied between different scenarios. In general, the water age for RWU was far longer in dry years (2003~2004) than in wet years (2005~2006), suggesting that drought can promote crop uptake of old water. In the same growing season, the water age for RWU was consistently lower in May and June than in July and August, which reflected an increase in the rooting depth.

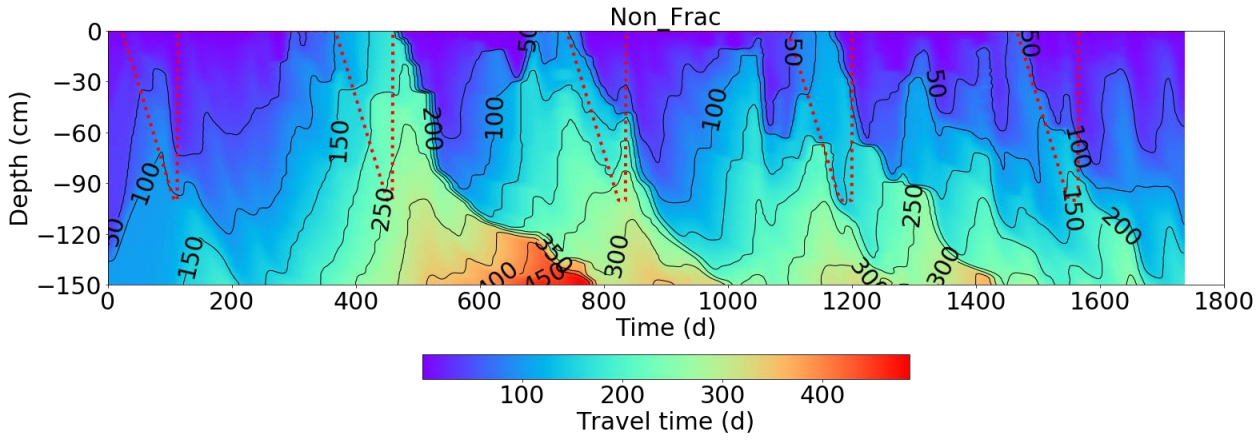

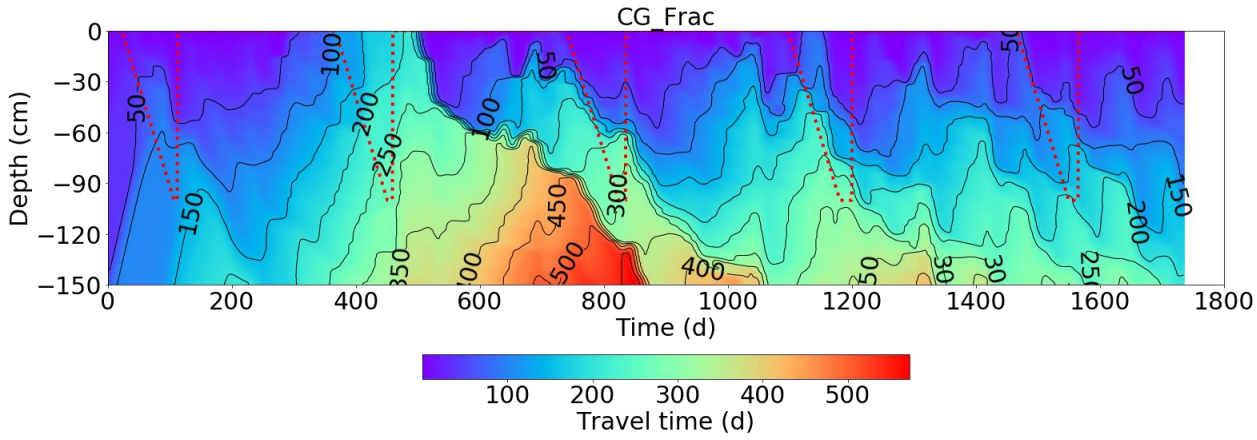

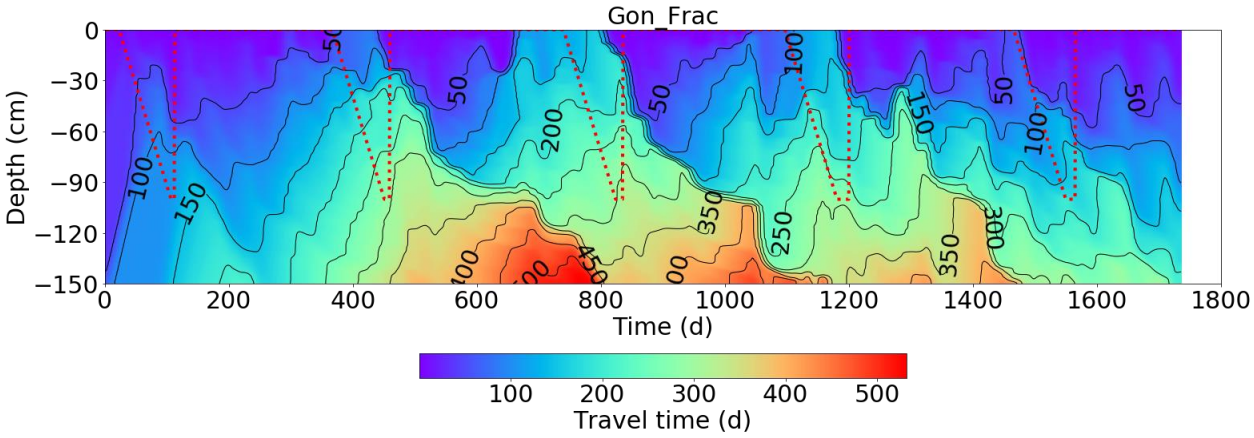

484

485 Figure 7. The residence time distributions (*RTD*s) for different fractionation scenarios (Non_Frac – top,

486 CG_Frac – middle, and Gon_Frac – bottom). Note that the dashed red line represents the rooting depth.

487

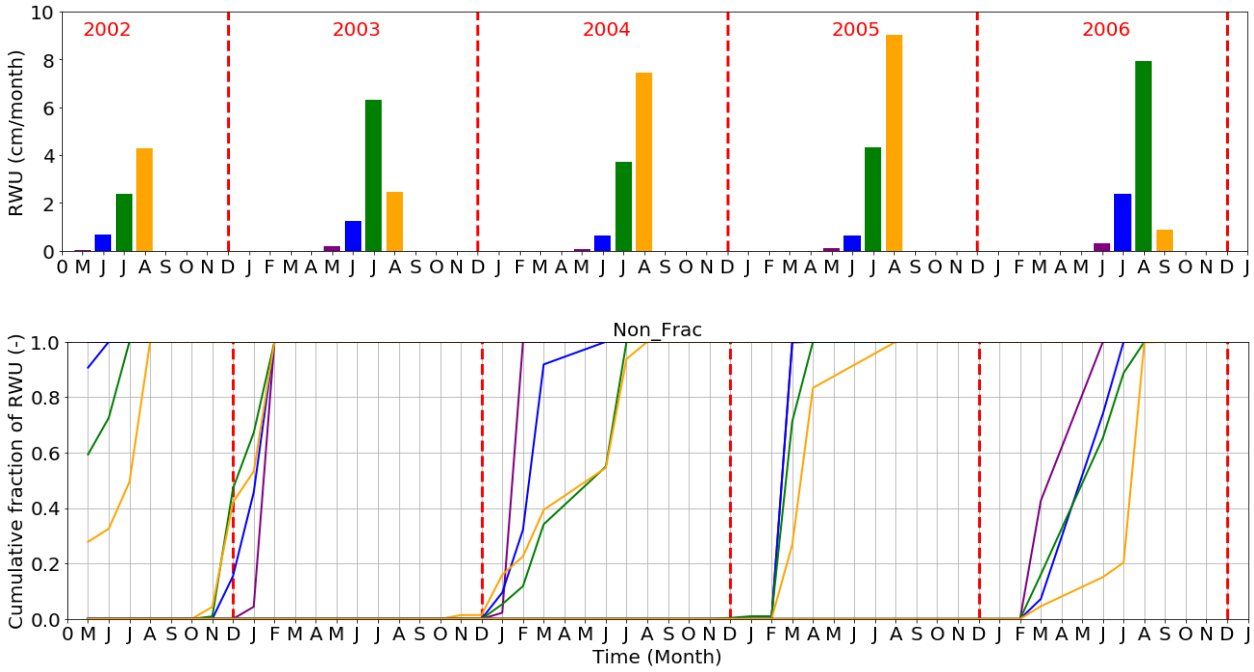

488

489

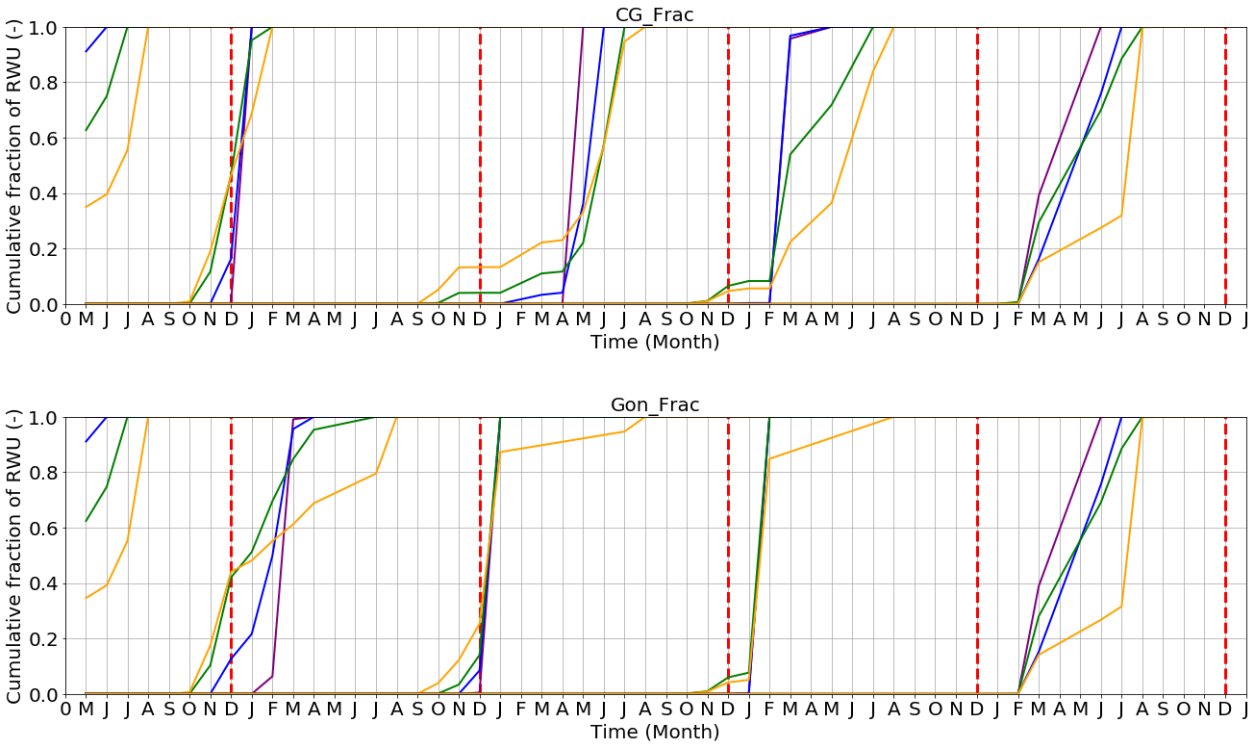

Figure 8. The temporal origin of root water uptake (RWU) for different fractionation scenarios (Non_Frac – top, CG_Frac – middle, and Gon_Frac – bottom). The upper panels show the monthly transpiration sums (in different colors); the lower panels show fractional contributions of water of a certain age/origin (by month) to the monthly transpiration sums.

3.2 Braud et al. (2009a) dataset analysis

3.2.1 Parameter optimization and model performance

The global sensitivity analysis and Monte-Carlo filtering results for the Braud et al. (2009a) dataset are shown in the Results S2 section of the Supplementary material. The most sensitive parameters were shape parameters n and saturated water contents θ_s. The final optimized soil hydraulic and solute transport parameters and corresponding KGEs are shown in Table 3. Considering (or not) evaporation fractionation also impacted parameter estimation significantly. The most significant impacts were on dispersivity,λ, and the shape parameter, α (Table 3). The soil water retention curves (Fig. S12) showed that the wilting points

were almost identical for the Non_Frac and fractionation (CG_Frac, Gon_Frac, Meas_Frac) scenarios. However, the saturated water contents were higher, and water contents started to drop later in the fractionation scenarios than those in the Non_Frac scenario. The soil hydraulic conductivity curves (Fig. S12) showed that the saturated hydraulic conductivities were very similar, but the hydraulic conductivities in the fractionation scenarios were a little higher than those in the Non_Frac scenario.

The fits of soil profile isotopic compositions for different fractionation scenarios are shown in Fig. 9. The Non_Frac scenario had an almost uniform isotopic composition profile. In this case, the parameter optimization depended mainly on the measured soil water content profile. In fractionation scenarios, the peak value of the isotopic composition profile in the Meas_Frac scenario was smaller than those in the Gon_Frac and CG_Frac scenarios, while the value of dispersivities was the opposite. Different fractionation scenarios resulted in significantly different average fitting performances (KGE_avg) (reached 0.72). The Meas_Frac scenario had the highest KGE_wi (i.e., for soil water isotopic composition), followed by Gon_Frac and CG_Frac scenarios, while the Non_Frac scenario performed the worst. The difference between KGE_wi indices for different fractionation scenarios reached 1.49.

Table 3. Optimized parameters and Kling-Gupta efficiency (KGE) indices (wc, wi, and avg refer to the water content, water isotopic composition, and average, respectively) for different fractionation scenarios (Non_Frac, CG_Frac, Gon_Frac, and Meas_Frac) (for the Braud et al. (2009a) dataset).

Fractionation scenario	θ_r cm^3/cm^3	θ_s cm^3/cm^3	α (cm^{-1})	n (-)	K_s (cm/d)	λ (cm)	KGE_wc	KGE_wi	KGE_avg
Non_Frac	0	0.435	0.0103	2.352	0.158	0.166	0.96	-0.55	0.20
CG_Frac	0	0.458	0.0106	2.367	0.139	0.126	0.85	0.37	0.61
Gon_Frac	0	0.441	0.0101	2.352	0.142	0.114	0.96	0.47	0.71
Meas_Frac	0	0.452	0.0082	2.392	0.156	0.932	0.90	0.94	0.92

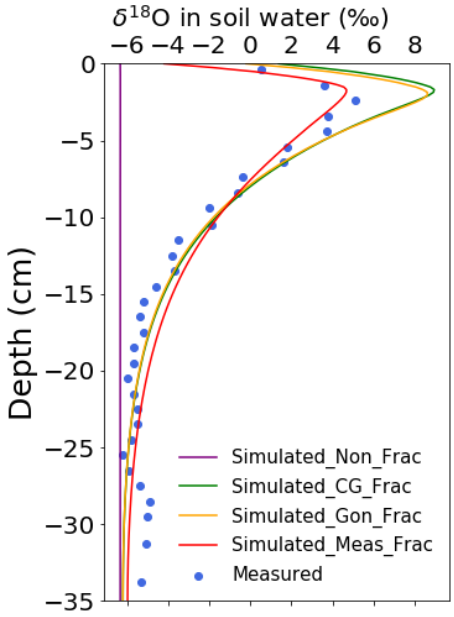

524

525 Figure 9. Measured (symbols) and simulated (lines) δ^{18}O isotopic compositions across the soil profile for
526 different fractionation (Non_Frac, CG_Frac, Gon_Frac, and Meas_Frac) scenarios (for the Braud et al.
527 (2009a) dataset).

528 **3.2.2 Second practical application: Estimation of evaporation flux**

529 Table 4 shows cumulative evaporation obtained using different measurements and simulated
530 considering different fractionation scenarios. The average isotopic composition of the whole profile was
531 calculated using soil water contents and the column depth as weights. Cumulative evaporation was estimated
532 to account for about 64.4%, 63.1%, and 65.6% of the initial soil water storage in the CG_Frac, Gon_Frac,
533 and Meas_Frac scenarios, respectively. These values for the CG_Frac, Gon_Frac, and Meas_Frac scenarios
534 were (slightly) lower than but comparable to laboratory measurements and the HYDRUS-1D water balance.
535 Slight differences may have been caused by uncontrollable measurement errors in the isotopic composition
536 of the atmospheric water vapor (δ_a in Eq. 5), which is the most sensitive parameter in the isotope mass
537 balance method (Skrzypek et al., 2015). Cumulative evaporation cannot be estimated using this method in
538 the Non_Frac scenario since no isotopic enrichment occurred (i.e., $\delta_s = \delta_0$ in Eq. 4).

539

Table 4. Cumulative evaporation measured using different experimental methods and calculated considering different fractionation scenarios.

Method	Fractionation scenario	Cumulative evaporation (mm)	Initial soil water storage (mm)	F_E (-)
Direct measurement (of airflow and humidity)		105	153	68.7%
Column weighting		103	153	67.1%
Trapped volume		103	153	67.3%
HYDRUS-1D water mass balance	Non_Frac	105	151	69.5%
	CG_Frac	105	159	66.0%
	Gon_Frac	105	153	68.6%
	Meas_Frac	105	157	66.9%
Isotope mass balance	Non_Frac	-	151	-
	CG_Frac	102	159	64.4%
	Gon_Frac	97	153	63.1%
	Meas_Frac	103	157	65.6%

Note that values of cumulative evaporation for the first three laboratory measurement methods are from Braud et al. (2009a).

4 Discussion

4.1 Impacts of evaporation fractionation on parameter estimation and model performance

For the Stumpp et al. (2012) dataset, as indicated in Section 3.1.1, the fractionation scenarios (CG_Frac and Gon_Frac) had lower hydraulic conductivities than the Non_Frac scenario. This is because fractionation decreases the isotope flux by evaporation compared with a no fractionation scenario (the isotopic composition of the evaporation flux cannot be greater than that of surface soil water) and thus increases the isotope flux by net infiltration. To get a good fit between simulated and observed isotopic compositions of discharge water, the inverse modeling yields a larger longitudinal dispersivity (to increase the dispersion of isotopes) (Table 1) or lower hydraulic conductivities (to decrease downward convection of isotopes) (Fig. S8).

The simulated isotopic composition of the lysimeter discharge remained the same for different fractionation scenarios during about the first 150 d and started deviating after this time (Fig. 6). This suggests

that it takes about 150 d before the impact of different treatments of the upper BC for isotope transport propagates to the soil profile bottom and affects the isotopic composition in drainage water (Zhou et al., 2021). This time interval (i.e., about 150 d) is much smaller than the travel time of the first particle (released at the soil surface) as calculated by the particle tracking method (Fig. S9). This is because the particle tracking algorithm considers only piston flow, while dispersion accelerates the arrival of isotopes to the soil profile bottom. However, the trends are still similar, except for some vertical shifts.

Since KGE_wi values did not differ much for different fractionation scenarios (within 0.09) (Fig. 6 and Table 1), considering (or not) evaporation fractionation does not significantly impact the isotopic composition in discharge water in this example (humid conditions). The Non_Frac scenario had a slightly higher KGE_wi, indicating that it can fit isotopic data better, followed by CG_Frac, while Gon_Frac performed the worst. This is understandable since evaporation fractionation could be neglected in this example, as seen from the dual-isotope plots (Fig. 5 of Stumpp et al., 2012).

For the Braud et al. (2009a) dataset, as indicated in Section 3.2.1, the hydraulic conductivities in the fractionation (CG_Frac, Gon_Frac, Meas_Frac) scenarios were a little higher than those in the Non_Frac scenario. This is because fractionation decreases the isotope flux by evaporation compared with a no fractionation scenario. A higher hydraulic conductivity in the fractionation scenarios promotes upward evaporation and fractionation. This increases the isotopic composition of remaining soil water and thus produces a better fit between simulated and observed isotope profiles.

When evaporation fractionation was not considered, the isotopic composition of evaporation remained the same as the initial isotopic composition. This resulted in a uniform isotopic composition (equal to the initial value) distribution of soil water throughout the profile in the Non_Frac scenario (Fig. 9). In fractionation scenarios, the peak value of the isotopic composition profile was inversely proportional to the dispersivity value (Fig. 9 and Table 3), which is consistent with the conclusions from Braud et al. (2009b).

The isotopic composition profiles and the KGE_wi values differed dramatically (reached 1.48) between different fractionation scenarios (Fig. 9 and Table 3). This implies that considering evaporation

fractionation significantly impacts the isotopic composition profile in this example (arid conditions). The Meas_Frac scenario had the highest KGE_wi (i.e., for the water isotopic composition), followed by the Gon_Frac, and then CG_Frac, while the Non_Frac scenario performed the worst. This is understandable since evaporation fractionation could not be neglected, and the measured evaporation isotope flux is the most accurate for this example (Braud et al. 2009b).

4.2 Impacts of evaporation fractionation on practical applications

4.2.1 Estimation of drainage and RWU travel times

Differences in water travel times were not evident among different fractionation scenarios (Table 4), since the numerator in Eq. 2 is much larger than the denominator in the peak displacement method. As a result, water travel times were similar for different fractionation scenarios despite a very different dispersivity. However, for the particle tracking method based on water flow calculations, differences in water travel times were evident among different fractionation scenarios (Table 2), despite their similar KGE values (Table 1). In addition, differences in estimated soil hydraulic parameters may also cause discrepancies in *TT*s of individual precipitation events and the temporal origin of water for RWU (Figs. S8 and 7~8).

Overall, the particle tracking method gave much higher travel times than the peak displacement method (Table 2). Different results by these two methods may be associated with different rainfall events selected for these calculations. The peak-displacement method calculates the travel times during frequent and heavy precipitation events (precipitation events from 2005~2006), while particle tracking assesses the travel times over longer periods (Zhou et al., 2021).

Notably, water travel times in the Non_Frac scenario obtained by the particle tracking method are most consistent with the approximate estimate of 41weeks provided by previous studies with similar crops and areas (Stumpp et al., 2009). It is worth mentioning that Asadollahi et al. (2020) pointed out that the SAS approach was a good alternative for estimating water travel times when the system was too complicated to be fully described by the HYDRUS-1D model. Our study demonstrates that the water-flow-based particle

tracking module in HYDRUS-1D is another promising way of constraining estimation errors in water travel times, especially when there is not enough isotope data to calibrate the lumped or physically based isotope transport models.

In contrast, considering fractionation using either the CG or Gonfiantini models will likely led to larger water travel time estimates than in the Non_Frac scenario (Table 2). This is because fractionation scenarios result in a larger dispersivity (to increase the dispersion of isotopes) or lower hydraulic conductivities (to decrease convection of isotopes), as discussed in Section 4.1.

4.2.2 Estimation of the evaporation flux

For evaporation estimation, the isotope-transport-based methods for different fractionation (CG_Frac, Gon_Frac, and Meas_Frac) scenarios can give comparable results to the water-flow-based methods, including laboratory measurements and the HYDRUS-1D water balance. In contrast, the Non_Frac scenario can produce similar results only when using the water-flow-based method (HYDRUS-1D water balance). However, since the measured evaporation flux was used as the upper boundary condition in this (arid conditions) example, it is not clear whether the similarity between estimated evaporation amounts using the HYDRUS-1D water balance method in the Non_Frac and fractionation (CG_Frac, Gon_Frac, Meas_Frac) scenarios was due to this boundary condition, or because actual soil hydraulic conductivities and water contents were continuously adjusted to actual soil fluxes without ever reaching full saturation. However, it is clear that evaporation fractionation has a significant impact on the isotope transport and isotopic compositions in arid conditions, as shown in Fig. 9. Therefore, the direct use of simulated isotopic compositions in the Non_Frac scenario may result in large biases in practical applications in arid conditions, as seen from the evaporation estimation results in Table 4.

4.3 Comparison of different climate conditions and implications for future studies

The soil saturated hydraulic conductivities (K_s), and the retention curve shape parameter (α) were the parameters most affected by the consideration of evaporation fractionation for the humid condition dataset (Table 1). For the arid condition dataset, these were the dispersivity (λ) and the retention curve shape

parameter (α) (Table 3). This is likely associated with the effects of soil texture on retention curves and soil moisture conditions in different climate zones (Radcliffe and Šimůnek, 2018). Overall, soil water retention and hydraulic conductivity curves (Fig. S12) in different fractionation scenarios were more similar for the Braud et al. (2009a) dataset than the Stumpp et al. (2012) dataset (Fig. S8). One reason is that the measured evaporation flux was used as the upper BC in the former, which constrains the model flexibility. Another reason is that there was only one soil layer in the Braud et al. (2009a) dataset, while there were three soil layers in the Stumpp et al. (2012) dataset. There is likely a compensation effect between the parameters of different layers, and thus the parameter values can vary more in the Stumpp et al. (2012) dataset.

While evaporation fractionation plays an essential role in parameter estimation in both cases, its impact on model performance is relatively small in the example for humid conditions but more significant in the example for arid conditions, as discussed in Sections 4.1 and 4.2. This is expected since evaporation plays a more important role in the water balance of the arid dataset (Table 4) than in the humid dataset (Fig. S13). These conclusions also indirectly validate the common assumption that evaporation fractionation may be neglected in some humid regions but not in arid areas (Sprenger et al., 2016a).

However, parameter sensitivities and optimization results reflect complex combined effects of climate, soil, and vegetation characteristics. The isotopic composition of soil water is not only affected by evaporation fractionation, but also by the mixing of rainfall with soil water and different flow paths in the soil, leading to its variations with depths and time. The insufficient knowledge of the spatiotemporal isotope distribution (e.g., in shallow and deep depths or during different stages of evaporation) and the lack of such information in the objective function may bias the parameter estimation results. For example, not including isotopes from different soil depths within the soil profile might lead to an underestimation of evaporation fractionation in general, biased estimation of water mixing within the profile, and a similar isotopic signal in the discharge. In this study, we considered either the time series of the isotopic composition of the bottom flux in the Stumpp et al. (2012) dataset or the final isotopic composition profile in the Braud et al. (2009a) dataset. In addition, observation data types and spatiotemporal distributions are different for these two

datasets, and this difference may affect the comparison of parameter estimation results between different climate conditions.

The GSA was carried out for the Non_Frac scenario for the Stumpp et al. (2012) dataset and the Meas_Frac scenario for the Braud et al. (2009a) dataset because they were closest to the experimental conditions. This implicitly assumes that sensitivity remains the same for different model structures. However, different model structures may affect GSA and PSO results, which should be further explored. Last but not least, the impacts of possible transpiration fractionation, as observed in multiple studies, should also be included in future analyses (e.g., Barbeta et al., 2019). Therefore, it is difficult to generalize the results of this study or apply them to other specific conditions.

5 Summary and Conclusions

In this study, we analyzed parameter estimation results for two datasets collected under humid and arid climate conditions using the isotope transport model, in which we either did or did not consider evaporation fractionation. The global sensitivity analysis using the Morris and Sobol' methods and the parameter estimation using the Particle Swarm Optimization algorithm highlight the significant impacts of considering evaporation fractionation on parameter estimation and model performance. The KGE index for isotope data can increase by 0.09 and 1.49 for the humid and arid datasets, respectively, when selecting suitable fractionation scenarios.

The impact of different parameter values estimated when considering (or not) evaporation fractionation propagates into practical applications of isotope transport modeling. The isotope-transport-based method (peak displacement) gave much lower water travel times than the water-flow-based method (particle tracking) for humid conditions. Considering fractionation using the CG and Gonfiantini models will likely lead to larger water travel time estimates and ages for RWU. For arid conditions example, the isotope-transport-based method (isotope mass balance) can provide comparable evaporation estimates for different fractionation (CG_Frac, Gon_Frac, Meas_Frac) scenarios as the water-flow-based methods

(HYDRUS-1D water balance and laboratory measurements). In contrast, the Non_Frac scenario can produce reasonable evaporation estimation only when using the water-flow-based method.

The direct use of simulated isotopic compositions in the no fractionation scenario may result in large biases in practical applications in arid regions where evaporation fractionation is more extensive than in humid areas. Integrated use of water-flow and isotope-transport-based methods may provide mutual validation and be an important way to avoid this problem. This research may shed some light on future laboratory and field experimental designs regarding the practical applications of the isotope-transport modeling in different climate zones.

Appendix

Acronym/Symbol	Description	Dimension/Units
P	Precipitation	L
ET_0	Grass-reference potential evapotranspiration	L
E	Actual evaporation	L
E_i	Isotope flux of evaporation	‰·L/T or ML^{-2}/T
T_s	Soil surface temperature	℃
T_{air}	Air temperature	℃
RH	Air relative humidity	-
LAI	Leaf area index	-
δ_P	Isotopic composition of precipitation	‰
δ_0	Initial isotopic composition of soil water	‰
δ_E	Isotopic composition of evaporation flux	‰
δ_s	Isotopic composition of the residual liquid	‰
δ^*	Limiting isotopic composition	‰
δ_A	Isotopic composition of the atmospheric water vapor	‰
xm	Enrichment slope	-
α^+	Equilibrium fractionation factor	-
ε^+	Equilibrium fractionation enrichment	‰
ε_k	Kinetic fractionation enrichment	‰
α_i^k	Kinetic fractionation factor at the soil surface	-
α_i^D	Kinetic fractionation factor within the soil	-
n_k	Kinetic fractionation coefficient within the soil	-
F_E	Ratio of the evaporation loss to the initial water storage	-
θ_r	Residual water content	L^3/L^3
θ_s	Saturated water content	L^3/L^3
n, α	Shape parameters of the VG model	-
K_s	Saturated hydraulic conductivity	L/T
λ	Longitudinal dispersivity	L

Acknowledgments

This research was financially supported by the Multistate W4188 program. We acknowledge Paolo Benettin from the Laboratory of Ecohydrology ENAC/IIE/ECHO, École Polytechnique Fédérale de Lausanne (EPFL), Lausanne, Switzerland, for his useful suggestions. We also appreciate the editors and reviewers for their constructive comments on this manuscript.

References

Allen, S.T., Kirchner, J.W., Braun, S., Siegwolf, R.T.W., Goldsmith, G.R., 2019. Seasonal origins of soil water used by trees. Hydrology and Earth System Sciences, 23(2): 1199-1210. DOI:10.5194/hess-23-1199-2019

Asadollahi, M., Stumpp, C., Rinaldo, A., Benettin, P., 2020. Transport and Water Age Dynamics in Soils: A Comparative Study of Spatially Integrated and Spatially Explicit Models. Water Resources Research, 56(3): 17. DOI:10.1029/2019wr025539

Barbeta, A., Jones, S. P., Clavé, L., Wingate, L., Gimeno, T. E., Fréjaville, B., Wohl, S., and Ogée, J., 2019. Unexplained hydrogen isotope offsets complicate the identification and quantification of tree water sources in a riparian forest. Hydrology and Earth System Sciences, 23(4): 2129-2146. DOI:10.5194/hess-23-2129-2019

Benettin, P., Bertuzzo, E., 2018. tran-SAS v1.0: a numerical model to compute catchment-scale hydrologic transport using StorAge Selection functions. Geosci. Model Dev., 11(4): 1627-1639. DOI:10.5194/gmd-11-1627-2018

Benettin, P., Rinaldo, A., Botter, G., 2015. Tracking residence times in hydrological systems: forward and backward formulations. Hydrological Processes, 29(25): 5203-5213. DOI:10.1002/hyp.10513

Benettin, P., Volkmann, T. H. M., von Freyberg, J., Frentress, J., Penna, D., Dawson, T. E., and Kirchner, J. W., 2018. Effects of climatic seasonality on the isotopic composition of evaporating soil waters. Hydrology and Earth System Sciences, 22(5): 2881-2890. DOI:10.5194/hess-22-2881-2018

Beven, K., Freer, J., 2001. Equifinality, data assimilation, and uncertainty estimation in mechanistic modelling of complex environmental systems using the GLUE methodology. Journal of Hydrology, 249(1-4): 11-29. DOI:10.1016/s0022-1694(01)00421-8

Bouhlel, M.A., Bartoli, N., Otsmane, A. and Morlier, J., 2016. Improving kriging surrogates of high-dimensional design models by Partial Least Squares dimension reduction, Struct. Multidiscip. Optim., 53(5), pp. 935-952, doi:10.1007/s00158-015-1395-9

Braud, I., Bariac, T., Biron, P., Vauclin, M., 2009a. Isotopic composition of bare soil evaporated water vapor. Part II: Modeling of RUBIC IV experimental results. Journal of Hydrology, 369(1-2): 17-29. DOI:10.1016/j.jhydrol.2009.01.038

Braud, I., Biron, P., Bariac, T., Richard, P., Canale, L., Gaudet, J. P., and Vauclin, M., 2009b. Isotopic composition of bare soil evaporated water vapor. Part I: RUBIC IV experimental setup and results. Journal of Hydrology, 369(1-2): 1-16. DOI:10.1016/j.jhydrol.2009.01.034

Brinkmann, N., Seeger, S., Weiler, M., Buchmann, N., Eugster, W., and Kahmen, A., 2018. Employing stable isotopes to determine the residence times of soil water and the temporal origin of water taken up by Fagus sylvatica and Picea abies in a temperate forest. New Phytologist, 219(4): 1300-1313. DOI:10.1111/nph.15255

Brunetti, G., Šimůnek, J., Piro, P., 2016. A comprehensive numerical analysis of the hydraulic behavior of a permeable pavement. Journal of Hydrology, 540: 1146-1161. DOI:10.1016/j.jhydrol.2016.07.030

Brunetti, G., Šimůnek, J., Turco, M., Piro, P., 2018. On the use of global sensitivity analysis for the numerical analysis of permeable pavements. Urban Water J., 15(3): 269-275. DOI:10.1080/1573062x.2018.1439975

Brunetti, G., Šimůnek, J., Turco, M., Piro, P., 2017. On the use of surrogate-based modeling for the numerical analysis of Low Impact Development techniques, Journal of Hydrology, 548, pp. 263-277, doi:10.1016/j.jhydrol.2017.03.013

Campolongo, F., Cariboni, J., Saltelli, A., 2007. An effective screening design for sensitivity analysis of large models. Environ. Modell. Softw., 22(10): 1509-1518. DOI:10.1016/j.envsoft.2006.10.004

Chesnaux, R., Stumpp, C., 2018. Advantages and challenges of using soil water isotopes to assess groundwater recharge dominated by snowmelt at a field study located in Canada. Hydrological Sciences Journal, 63(5): 679-695. DOI:10.1080/02626667.2018.1442577

Condon, L.E., Atchley, A.L., Maxwell, R.M., 2020. Evapotranspiration depletes groundwater under warming over the contiguous United States. Nature Communications, 11(1): 8. DOI:10.1038/s41467-020-14688-0

Craig, H., Gordon, L., 1965. Deuterium and oxygen 18 variations in the ocean and the marine atmosphere, Stable Isotopes in Oceanographic Studies and Paleotemperatures E, Proceedings of the Third Spoleto Conference, Spoleto, Italy, pp. 9-130.

Gatel, L., Lauvernet, C., Carluer, N., Weill, S., Tournebize, J., and Paniconi, C., 2019. Global evaluation and sensitivity analysis of a physically based flow and reactive transport model on a laboratory experiment. Environ. Modell. Softw., 113: 73-83. DOI:10.1016/j.envsoft.2018.12.006

Gonfiantini, R., 1986. Environmental isotopes in lake studies. Handbook of Environmental Isotope Geochemistry, 2: 113-168.

Groh, J., Stumpp, C., Lücke, A., Pütz, T., Vanderborght, J., and Vereecken, H., 2018. Inverse Estimation of soil hydraulic and transport parameters of layered soils from water stable isotope and lysimeter data. Vadose Zone Journal, 17(1): 19. DOI:10.2136/vzj2017.09.0168

Harman, C.J., 2015. Time-variable transit time distributions and transport: Theory and application to storage-dependent transport of chloride in a watershed. Water Resources Research, 51(1): 1-30. DOI:10.1002/2014wr015707

Herman, J., Usher, W., 2017. SALib: an open-source Python library for sensitivity analysis. Journal of Open Source Software, 2(9): 97. DOI:10.21105/joss.00097

Herman, J.D., Kollat, J.B., Reed, P.M., Wagener, T., 2013. Technical Note: Method of Morris effectively reduces the computational demands of global sensitivity analysis for distributed watershed models. Hydrology and Earth System Sciences, 17(7): 2893-2903. DOI:10.5194/hess-17-2893-2013

Hopmans, J.W., Šimůnek, J., Romano, N., Durner, W., 2002. 3.6. 2. Inverse Methods. Methods of Soil Analysis: Part 4 Physical Methods, 5: 963-1008.

Knoben, W.J.M., Freer, J.E., Woods, R.A., 2019. Technical note: Inherent benchmark or not? Comparing Nash-Sutcliffe and Kling-Gupta efficiency scores. Hydrology and Earth System Sciences, 23(10): 4323-4331. DOI:10.5194/hess-23-4323-2019

Koeniger, P., Gaj, M., Beyer, M., Himmelsbach, T., 2016. Review on soil water isotope-based groundwater recharge estimations. Hydrological Processes, 30(16): 2817-2834. DOI:10.1002/hyp.10775

Liang, G., 1982. Net radiation, potential and actual evapotranspiration in Austria. Archives for Meteorology, Geophysics, and Bioclimatology, Series B, 31(4): 379-390.

Liu, D., Li, L.Z., Rostami-Hodjegan, A., Bois, F.Y., Jamei, M., 2020. Considerations and caveats when applying global sensitivity analysis methods to physiologically based pharmacokinetic models. AAPS J., 22(5): 13. DOI:10.1208/s12248-020-00480-x

Mattei, A., Goblet, P., Barbecot, F., Guillon, S., Coquet, Y., and Wang, S., 2020. Can soil hydraulic parameters be estimated from the stable isotope composition of pore water from a single soil profile? Water, 12(2): 19. DOI:10.3390/w12020393

Mertens, J., Stenger, R., Barkle, G.F., 2006. Multiobjective inverse modeling for soil parameter estimation and model verification. Vadose Zone Journal, 5(3): 917-933. DOI:10.2136/vzj2005.0117

781 Miguez-Macho, G., Fan, Y., 2021. Spatiotemporal origin of soil water taken up by vegetation. Nature: 17.
782 DOI:10.1038/s41586-021-03958-6
783 Nelson, J.A., Pérez-Priego, O., Zhou, S., Poyatos, R., Zhang, Y., Blanken, P.D., Gimeno, T.E., Wohlfahrt,
784 G., Desai, A.R., Gioli, B. and Limousin, J.M., 2020. Ecosystem transpiration and evaporation:
785 Insights from three water flux partitioning methods across FLUXNET sites. Glob. Change Biol.,
786 26(12): 6916-6930. DOI:10.1111/gcb.15314
787 Nossent, J., Elsen, P., Bauwens, W., 2011. Sobol' sensitivity analysis of a complex environmental model.
788 Environ. Modell. Softw., 26(12): 1515-1525. DOI:10.1016/j.envsoft.2011.08.010
789 Penna, D., Hopp, L., Scandellari, F., Allen, S.T., Benettin, P., Beyer, M., Geris, J., Klaus, J., Marshall, J.D.,
790 Schwendenmann, L. and Volkmann, T.H., 2018. Ideas and perspectives: Tracing terrestrial
791 ecosystem water fluxes using hydrogen and oxygen stable isotopes - challenges and opportunities
792 from an interdisciplinary perspective. Biogeosciences, 15(21): 6399-6415. DOI:10.5194/bg-15-
793 6399-2018
794 Radcliffe, D.E., Šimůnek, J., 2018. Soil physics with HYDRUS: Modeling and applications. CRC Press.
795 Ratto, M., Tarantola, S., Saltelli, A., 2001. Sensitivity analysis in model calibration: GSA-GLUE approach.
796 Comput. Phys. Commun., 136(3): 212-224. DOI:10.1016/s0010-4655(01)00159-x
797 Razavi, S., A. Jakeman, A. Saltelli, C. Prieur, B. Iooss, E. Borgonovo, E. Plischke, S. Lo Piano, T. Iwanaga,
798 W. Becker, S. Tarantola, J.H.A. Guillaume, J. Jakeman, H. Gupta, N. Melillo, G. Rabitti, V.
799 Chabridon, Q.Y. Duan, X.F. Sun, S. Smith, R. Sheikholeslami, N. Hosseini, M. Asadzadeh, A. Puy,
800 S. Kucherenko, and H.R. Maier, 2021. The future of sensitivity analysis: An essential discipline for
801 systems modeling and policy support, Environ. Modell. Softw., 137, pp. 22,
802 doi:10.1016/j.envsoft.2020.104954
803 Rinaldo, A., Benettin, P., Harman, C.J., Hrachowitz, M., McGuire, K.J., Van Der Velde, Y., Bertuzzo, E.
804 and Botter, G., 2015. Storage selection functions: A coherent framework for quantifying how
805 catchments store and release water and solutes. Water Resources Research, 51(6): 4840-4847.
806 DOI:10.1002/2015wr017273
807 Sheikholeslami, R., Razavi, S. and Haghnegahdar, A., 2019. What should we do when a model crashes?
808 Recommendations for global sensitivity analysis of Earth and environmental systems models,
809 Geosci. Model Dev., 12(10), pp. 4275-4296, DOI:10.5194/gmd-12-4275-2019
810 Shi, Y.H., Eberhart, R., 1998. A modified particle swarm optimizer, IEEE International Conference on
811 Evolutionary Computation. Ieee, Anchorage, Ak, pp. 69-73. DOI:10.1109/icec.1998.699146
812 Šimůnek, J., 1991. Numerical simulation of the transport processes in soil. Vodohospodarsky Casopis
813 (CSFR).
814 Šimůnek, J., Šejna, M., Saito, H., Sakai, M., van Genuchten, M.T., 2008. The HYDRUS-1D Software
815 Package for Simulating the One-Dimensional Movement of Water, Heat, and Multiple Solutes in
816 Variably Saturated Media, Version 4.0. HYDRUS Software Series 3. Department of Environmental
817 Sciences, University of California Riverside, Riverside, California, USA, 315 pp.
818 Skrzypek, G., Mydłowski, A., Dogramaci, S., Hedley, P., Gibson, J. J., and Grierson, P. F., 2015. Estimation
819 of evaporative loss based on the stable isotope composition of water using Hydrocalculator. Journal
820 of Hydrology, 523: 781-789. DOI:10.1016/j.jhydrol.2015.02.010
821 Sobol, I.M., 2001. Global sensitivity indices for nonlinear mathematical models and their Monte Carlo
822 estimates. Math. Comput. Simul., 55(1-3): 271-280. DOI:10.1016/s0378-4754(00)00270-6
823 Sprenger, M., Leistert, H., Gimbel, K., Weiler, M., 2016a. Illuminating hydrological processes at the soil-
824 vegetation-atmosphere interface with water stable isotopes. Reviews of Geophysics, 54(3): 674-704.
825 DOI:10.1002/2015rg000515
826 Sprenger, M., Seeger, S., Blume, T., Weiler, M., 2016b. Travel times in the vadose zone: Variability in
827 space and time. Water Resources Research, 52(8): 5727-5754. DOI:10.1002/2015wr018077
828 Sprenger, M., Volkmann, T.H., Blume, T., Weiler, M., 2015. Estimating flow and transport parameters in
829 the unsaturated zone with pore water stable isotopes. Hydrology and Earth System Sciences.

Stumpp, C., Maloszewski, P., Stichler, W., Fank, J., 2009. Environmental isotope (delta O-18) and hydrological data to assess water flow in unsaturated soils planted with different crops: Case study lysimeter station "Wagna" (Austria). Journal of Hydrology, 369(1-2): 198-208. DOI:10.1016/j.jhydrol.2009.02.047

Stumpp, C., Stichler, W., Kandolf, M., Šimůnek, J., 2012. Effects of land cover and fertilization method on water flow and solute transport in five lysimeters: A long-term study using stable water isotopes. Vadose Zone Journal, 11(1): 14. DOI:10.2136/vzj2011.0075

Sutanto, S.J., Wenninger, J., Coenders-Gerrits, A.M.J., Uhlenbrook, S., 2012. Partitioning of evaporation into transpiration, soil evaporation and interception: a comparison between isotope measurements and a HYDRUS-1D model. Hydrology and Earth System Sciences, 16(8): 2605-2616. DOI:10.5194/hess-16-2605-2012

Timbe, E., Windhorst, D., Crespo, P., Frede, H. G., Feyen, J., and Breuer, L., 2014. Understanding uncertainties when inferring mean transit times of water trough tracer-based lumped-parameter models in Andean tropical montane cloud forest catchments. Hydrology and Earth System Sciences, 18(4): 1503-1523. DOI:10.5194/hess-18-1503-2014

Vrugt, J.A., Robinson, B.A., 2007. Improved evolutionary optimization from genetically adaptive multimethod search. Proc. Natl. Acad. Sci. U. S. A., 104(3): 708-711. DOI:10.1073/pnas.0610471104

Vrugt, J.A., Stauffer, P.H., Wohling, T., Robinson, B.A., Vesselinov, V.V., 2008. Inverse modeling of subsurface flow and transport properties: A review with new developments. Vadose Zone Journal, 7(2): 843-864.

Wohling, T., Vrugt, J.A., 2011. Multiresponse multilayer vadose zone model calibration using Markov chain Monte Carlo simulation and field water retention data. Water Resources Research, 47: 19. DOI:10.1029/2010wr009265

Wollschlager, U., Pfaff, T., Roth, K., 2009. Field-scale apparent hydraulic parameterisation obtained from TDR time series and inverse modelling. Hydrology and Earth System Sciences, 13(10): 1953-1966. DOI:10.5194/hess-13-1953-2009

Zhou, T., Šimůnek, J., Braud, I., 2021. Adapting HYDRUS-1D to simulate the transport of soil water isotopes with evaporation fractionation. Environ. Modell. Softw., 143: 18. DOI:10.1016/j.envsoft.2021.105118